APPROACHES TO IMAGING FEEDZONE DIVERSITY WITH CASE STUDIES FROM SUMATRA, INDONESIA AND THE TAUPŌ VOLCANIC ZONE, NEW ZEALAND

Irene Wallis[1], Julie Rowland[1], David Dempsey[2], George Allan[4], Ridwan Sidik[3], Rudy Martikno[3], Katie McLean[5], Mauliate Sihotang[3], Herwin Azis[3], Marino Baroek[3]

[1] School of Environment, University of Auckland, 23 Symonds Street, Auckland Central, New Zealand

[2] Engineering Science, University of Auckland, 70 Symonds Street, Auckland Central, New Zealand

[3] PT Supreme Energy, Menara Sentraya, 23rd Floor. Jl. Iskandarsyah Raya No 1A, Jakarta 12160, Indonesia

[4] Mercury, 283 Vaughan Road, Rotorua, New Zealand

[5] Contact Energy, Ltd, Private Bag 2001, Taupo 3352, New Zealand

i.wallis@auckland.ac.nz

Keywords: *Rantau Dedap, Muara Laboh, Ngatamariki, Wairakei, borehole image log, fracture, geomechanics*

ABSTRACT

There is a fast-growing inventory of studies on borehole image logs acquired in geothermal reservoirs as more operators elect to deploy this technology. Our contribution to this inventory is to illustrate how judicious use of these data may reveal the geologic controls on permeability. We also provide an open source Python library that enables others to replicate the methods described herein. Our study includes a discussion of geometric sample bias, as well as those data integrity and geological factors that influence fracture frequency. We also demonstrate slip tendency modelling as an approach to identifying fractures that may be relevant beyond the borehole wall, which is key for geothermal wells where thermal stresses have enhanced both the number and apparent aperture of fractures at the borehole wall. We illustrate these methods using seven well case studies from a wide range of lithologies, four reservoirs, and two tectonic settings—one dominated by a volcano-tectonic rift and the other a mega-shear zone. The reservoirs are Muara Laboh and Rantau Dedap in Indonesia and Ngatamariki and Wairakei in New Zealand.

1. INTRODUCTION

We use seven case study boreholes from four reservoirs that are located in two geothermal districts to critically evaluate aspects of image log interpretation methodology for high-temperature geothermal wells (Figure 1 and Table 1). Many studies use borehole image logs to investigate controls on fluid flow (e.g., Davatzes and Hickman, 2010a; Hickman et al., 1997; Massiot et al., 2017b; McNamara et al., 2015; Nemčok et al., 2007; Stimac et al., 2010), but they rarely include multiple reservoirs or explicitly address the absolute magnitude of well permeability. Our study departs from this tradition in an effort to quantify the geologic controls on the diversity of feedzones (FZ) that a geothermal developer may encounter (or seek to encounter) because accurate quantification generates improved prediction.

Table 1: Case study reservoirs

Reservoir	Installed MWe	First generation
Rantau Dedap (RD)	90	Under construction
Muara Laboh (ML)	85	2019
Ngatamariki (NM)	82	2013
Wairakei (WK)	175 + 166	1958

In this paper, we discuss both the appropriateness of and challenges with using FZ rather than temperature as comparative data in image interpretation studies. We describe the value of including geologic and hydrologic context when interpreting image logs before focusing on issues surrounding analysis of the fracture data derived from image logs acquired in high-temperature, geothermal wells. We showcase a method for visualizing geometric sample bias and illustrate the effectiveness of slip tendency modelling. Finally, using one case study as an example, we demonstrate that judicious use of image log data, where both geologic complexity and data integrity are considered, generates insight into the geologic mechanisms that control high-magnitude permeability and, therefore, the distribution of FZ.

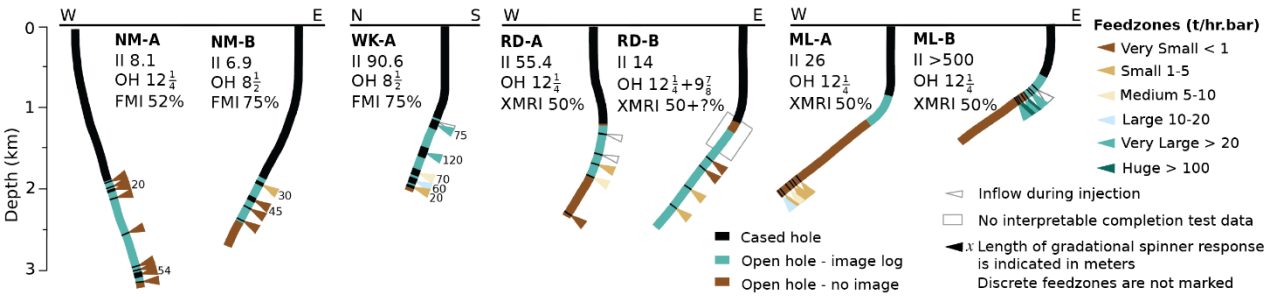

Figure 1: Case study wells. II = injectivity index (t/hr.bar), OH = open hole diameter (inches). Micro-resistivity image log tool types are Schlumberger Fullbore Formation Microimager (FMI) and Halliburton X-tended Range Micro Imager (XMRI), where percentage is the proportion of the well circumference that is imaged given the size of the well and the tool type.

ISSN 2703-4275

2. DEFINING FEEDZONES

Studies of very low permeability wells yield good results from comparison between log data and fine-scale fluctuations in static temperature (e.g., Barton et al. 1995; Davatzes and Hickman 2010). In high-temperature geothermal wells where high-magnitude flows and complex internal well dynamics (e.g., interzonal flows) can be present, we prefer to compare log data with the distribution of feedzones (refer to Zarrouk and McLean, 2019 for feedzone interpretation methods). A FZ is where detectable quantities of mass (steam or liquid) flux into or out of the wellbore, which may or may not cause disturbance in measured temperature. Mass flux through a FZ is a function of the difference between pressure in the reservoir and well, fluid viscosity and density, and permeability. Only the latter relates to geologic context. Hanano (2004) proposed that FZ require a local high in horizontal permeability > 10^{-12} m^2, which is several orders of magnitude larger than the range of vertical permeability that is sufficient for the onset of convection (10^{-15} to 10^{-16} m^2, depending on fluid temperature/buoyancy). FZ are typically identified using a combination of temperature and fluid velocity profiles measured at multiple injection rates and pressure profiles acquired as the well heats up after injection ceases. Utilisation of all data types available in the interpretation is best practice because the data may not resolve a particular FZ. For instance, there is a tendency to overlook shallower FZ in favour of deeper ones because the spinner response under injection to deep FZ is empathised by the greater pressure difference between the wellbore and reservoir at depth. Temperature data, especially those acquired as the well heats, may better resolve the depth of shallow FZ.

Figure 1 plots the FZ distribution of the case study wells from Muara Laboh (ML) and Rantau Dedap (RD) in Indonesia and Ngatamariki (NM) and Wairakei (WK) in New Zealand. FZ are interpreted from completion testing split into categories based on magnitude so that comparisons can be made between wells. However, this distribution is dynamic in response to well operating conditions. Dominantly due to changing the pressure gradient between the well and reservoir, injection and production testing may result in a different relative magnitude or spatial distribution of FZ. Sometimes a shallow FZ that either accepted a minor proportion of injection fluid or produced during the completion test (e.g., WK-A, RD-A, and ML-B) will increase in relative contribution when a well is flowed. In contrast, the deepest FZ identified in the completion test may contribute proportionately less to production. This is because a relatively large pressure difference forms at depth between the well and reservoir under cold water injection.

Given the that geothermal wells are prone to have borehole intervals larger than the bit size, accurate detection of very small FZ (< 1 t/hr.bar) is difficult, particularly when nearby large (>20 t/hr.bar) or very large (> 100 t/hr.bar) FZ dominate the flow behaviour. Very small FZ may stimulate in response to injection. Alternatively, depending on temperature, pressure and connectivity to the wider reservoir, they may or may not contribute appreciably to production. Given these uncertainties, we place less weight on correlations between geologic context and very small FZ, in particular those at the bottom of wells.

The distribution and magnitude of FZ may also evolve during a well's lifetime in response to mineral deposition or dissolution, pressure or thermally induced stimulation, or evolution of pressure, temperature and phase in the reservoir. As completion tests are typically done around the same time as image log acquisition, with NM-A the exception in this set of case studies, these are the natural data for comparison. Connectivity between a FZ and the wider reservoir influences sustainable production and may affect how an injection well responds to thermal stimulation. Therefore, to understand FZ we must also consider conditions beyond the borehole wall. A complete understanding therefore encompasses short and long-term production test data where available, information on connectivity to the reservoir (e.g., pressure transient testing), and acknowledges the dynamic nature of FZ in permeable, high-temperature geothermal wells.

3. GEOLOGIC CONTEXT

There are three scales of geologic context to consider when interpreting image log data: the regional, reservoir and wellbore scale. We use this context to make sense of features observed in image logs and to provide reasonable bounds for our models. Later integration of results from log data interpretation may improve the depth accuracy and overall resolution for some aspects of contextual data (e.g., the geologic and conceptual models).

3.1 Case Study Context

The case studies are located in two contrasting tectonic settings (Figure 2). We use this district-scale context to generate reasonable bounds for the geomechanical models and the explanatory structural models for the pattern of geology observed at the borehole wall. The Great Sumatra Fault Zone, Indonesia (GSF) is a ~1660 km long, segmented, right-lateral, strike-slip fault system which is coincident with a volcanic arc (Figure 2: Sieh and Natawidjaja, 2000). ML and RD are both located in the southern domain of the GSF and the former lies within a step-over between two segments of the GSF (Sidik et al., 2018). RD is located ~15 km east of the GSF trace and may be localized by interaction between northwest-striking inherited basement structure and splays from the GSF. The Taupō Volcanic Zone, New Zealand (TVZ) is a ~300 km long active volcano-tectonic rift whose central domain is exceptional for the magnitude of volcanic and geothermal productivity (Ellis et al., 2014; Wilson and Rowland, 2016). Rift extension ranges from ~10-15 mm/year and is accommodated by a series of NE-striking rift segments and NW-to-NNW trending transfer zones (Rowland and Sibson, 2004). NM and WK are ~ 10 km apart, with the former located on what is thought to be the shoulder of the buried Whakamaru caldera while the latter is situated within the caldera fill (Rosenberg et al., 2020).

The reservoir-scale geologic setting and conceptual models are well described elsewhere: RD (Mussofan et al., 2019; Sidik et al., 2018), ML (Stimac et al., 2019a; Stimac et al., 2019b), NM (Chambefort et al., 2016), and WK (Bixley et al., 2009; Rosenberg et al., 2020; Sepulveda et al., 2012). Previous studies using log data from these reservoirs include: RD (Sidik et al., 2016), ML (Baroek et al., 2018; Mussofan et al., 2019), NM (Halwa et al., 2013; Wallis et al., 2012), and WK (Massiot et al., 2017a; McNamara et al., 2016; McNamara et al., 2019). Although the litho-types intersected are similar, the logs from GSF and TVZ include different aged rocks with a contrasting degree of variation in their tectonic histories. Where the TVZ case studies are logs from Quaternary-aged rock formed under reasonably consistent

tectonic conditions, the GSF case studies include Miocene-aged rock that has experienced a long history of inversion tectonics. Where secondary fracture orientations are not consistent with surface fault mapping or the current tectonic context, this overprinted history may be the cause. We use faults that are constrained by data independent of the image logs, such as geologic offset, surface mapping, and geophysical methods like microseismicity or gravity to support image log interpretation. Structures that meet these criteria are intersected by NM-B and RD-B.

All case study wells aside from NM-A and NM-B are completed into the production reservoir sector. However, all wells are pressure connected to production and include a significant interval of hot, nearly-isothermal thermal gradient that indicates convective conditions. All case study logs correlate with measured temperatures and fluid chemistry that equate with a propylitic alteration assemblage, but some log intervals include relic phyllic assemblages. Micro-resistivity images provide limited data about the spatial extent of alteration because fractures with resistive mineral fill appear as bright sinusoids and those with highly conductive mineral fill are dark sinusoids with haloing from electrical current accumulation (Figure 3D). Care should be taken not to confuse the latter with cases where an alteration halo dominated by resistive minerals has formed around a fracture.

At the wellbore scale, the sequence of lithology has been depth-corrected using the textural variation in micro-resistivity image logs and the petrophysical facies approach in those wells where a range of petrophysical logs were acquired (NM-A and NM-B; Wallis et al., 2012). Application of standard petrophysical relations between log response and porosity require care when using data acquired from geothermal reservoirs because of the impact hydrothermal alteration has on rock properties, but experimental studies have demonstrated that they work (Durán et al., 2019). Subsequently, these petrophysical logs, which can be acquired at the same time as the image log with little impact on rig time, provide quantitative, depth-accurate data on bulk mineral composition and porosity which adds significant value to image log interpretation. The depth correction of geologic contacts is typically > 10-30 m, depending on the well hydrology during drilling and casing arrangement (i.e., in-well volume and therefore velocity change caused by hung liners). In some cases, we used logs to define the lithological sequence where no cuttings were returned to surface or to identify units that were not resolved by hand-specimen description of cuttings (e.g., Figure 3E).

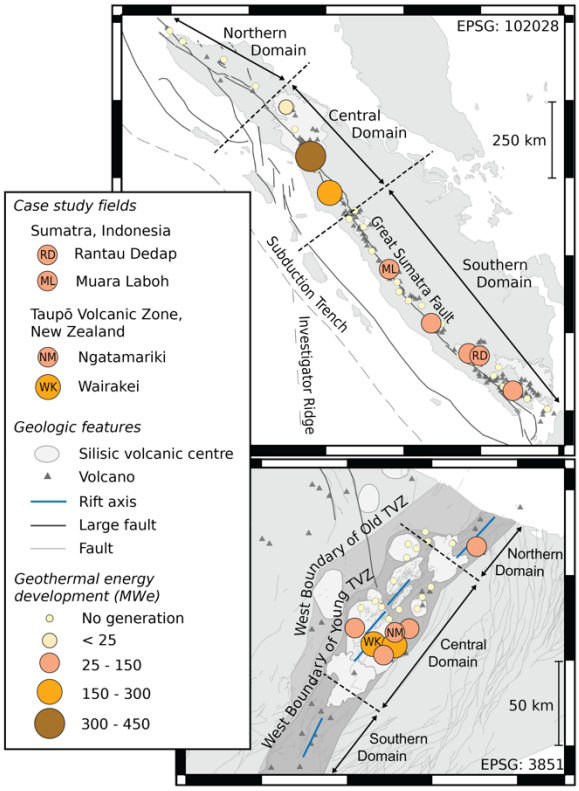

Figure 2: Case study reservoirs within their regional volcano-tectonic setting. Figure adapted from Wallis et al. (2018) and references therein.

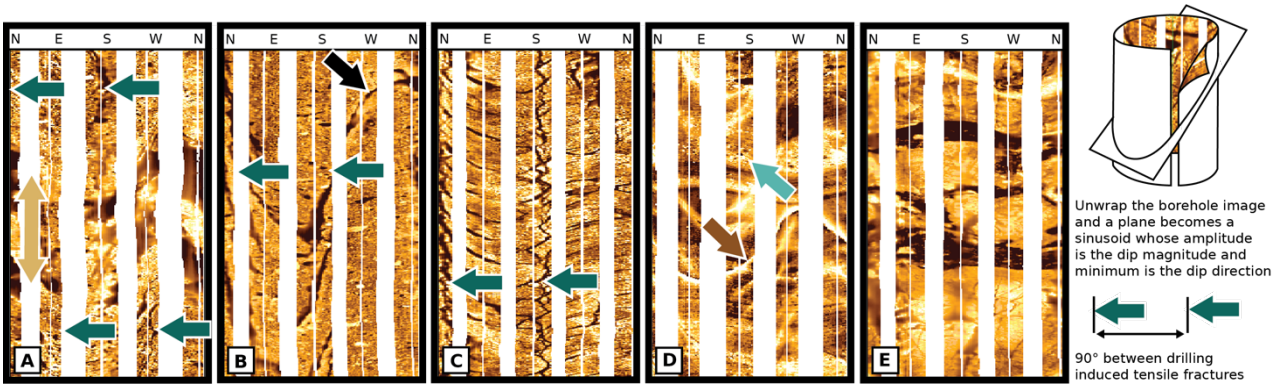

Figure 3: Examples of features recognised in micro-resistivity image logs, where the relative electrical resistivity of the borehole wall is plotted from conductive (dark) to resistive (light). (A) The azimuth of drilling induced tensile fractures rotate as the well passes through an an almost 1 m thick fault (brown arrow). (B) En echelon drilling-induced tensile fractures interact with a drilling enhanced natural fracture (black arrow). (C) Parallel, low-amplitude conductive (dark) sinusoids along andesite flow banding are likely to be only open at the borehole wall in response to thermally-amplified tensile hoop stress (i.e., are thermally induced fractures). (D) Bright halos (e.g., dark brown arrow) indicate current accumulation around fractures filled with highly conductive minerals (e.g., pyrite) and, less commonly, disseminated alteration within particular geologic layers (blue arrow). (E) Volcaniclastic unit not recognisable in cuttings because it is dominantly comprised of large (>20 cm) andesite clasts in clay-rich matrix. Examples are from NMB and the depth of panels A-E are plotted in Figure 6.

4. FRACTURE FREQUENCY DATA

At first glance, the frequency of fractures imaged along the well path may appear to be a simple method for making sense of the data yielded from image logs. However, variation in fracture frequency may reflect reservoir conditions or they may be the result of geomechanical processes at the wellbore wall or data acquisition issues such as geometric sample bias and image quality.

4.1 Data Integrity and Geometric Sample Bias

The reliability of fracture frequency data derived from borehole image interpretation is affected by quality and coverage of the image, geometric sample bias, and misclassification of drilling induced damage as natural fractures.

A range of issues impact the quality and borehole coverage of micro-resistivity images. As can be seen in Figure 3, micro-resistivity images are acquired in stripes where pads contact the borehole wall. If there is a lot of whitespace due to large completion sizes (c.f. Figure 1 for details on borehole coverage) or pad spacing is irregular due to issues with tool centralization, then azimuthal confidence of fractures picked from the image is reduced, as is our ability to resolve geomechanical features like borehole breakout and tensile fractures. This means that, while micro-resistivity images provide invaluable textural information that enables us to further resolve lithological sequences, acoustic borehole images are more suited to geomechanical studies.

Oversized or ovoid hole exasperates these coverage issues and, where pads lose contact with the borehole wall, it may lead to total image loss. However, micro-resistivity logs are less impacted by these conditions than acoustic logs because pads will maintain contact with the borehole wall in circumstances that would have already resulted in signal loss for an acoustic tool. Artefacts associated with sudden changes in logging speed and extreme resistivity contrast between mud and the borehole wall may also negatively impact readability of micro-resistivity images. Considering image quality along with fracture frequency enables us to discern variation that is simply due to the image.

Seminal work by Terzaghi (1965) revealed a geometric bias generated by sampling a three-dimensional fracture network with a line. Simply put, fractures planes that are perpendicular to the line are very likely to be intersected whereas those parallel to the line are almost never intersected. They proposed a methodology that corrects for the sample bias where a weighting is applied depending on the acute angle between the fracture plane and the well (equation in Figure 5). However, results can mislead interpretation by emphasizing solitary fractures that are not part of some significant but under-sampled population, especially where the weighting factor approaches infinity near sin $\alpha = 0$. Priest (1993) recommends resolving this by using an upper limit of sin $\alpha = 0.1$ when weighting.

There is a critical issue with these methods of correcting fracture populations: If a fracture has not been sampled, then it is not available for weighting. As can be seen in Figure 5, a well rarely insects fracture orientations that lie at sin $\alpha = 0 \pm 0.3$, unless there is a strong fracture cluster (e.g., NM-B). Plotting data with isogenic contours enables us to discern how badly geometric sample bias impacts our data. For instance, the weak cluster of fractures imaged in ML-B may have been interpreted as evidence for a structural grain. As fracture orientations lie almost exclusively within the sin $\alpha = 0.9$ contour, a judicious interpretation is that this pattern is more sample bias than geologic phenomena.

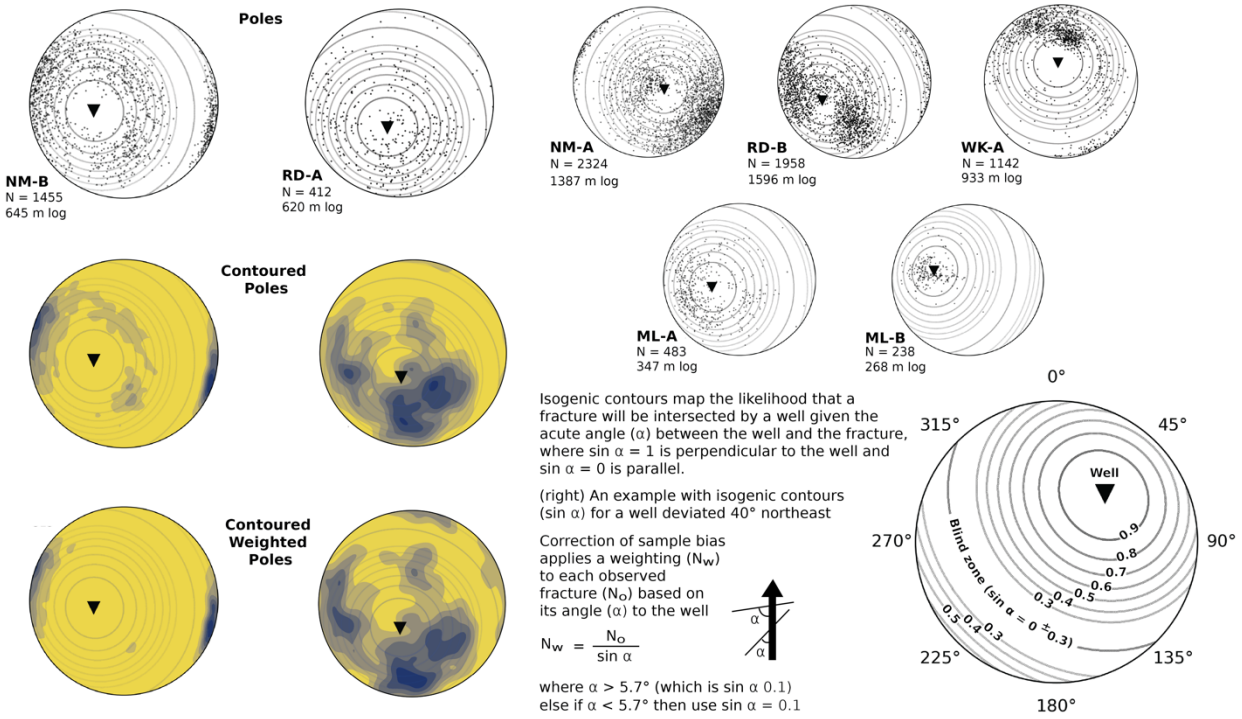

Figure 4: Stereonets with poles (the normal) to the fracture plane plotted for only those features that are possibly open (i.e., electrically conductive sinusoids without halos). Isogenic contours are constructed using the mean well azimuth and deviation in the logged interval. Methodology from Terzaghi (1965) and Priest (1993).

Thermal stress must be considered when interpreting image log data acquired in geothermal wells. A > 200°C difference between the reservoir and injected fluid is common, so extreme thermal stresses form at the wellbore wall. We conducted experiments using the Kirsh equations to investigate the impact of large temperature differences on stress at the wellbore wall (Jaeger et al., 2007). In a normal faulting environment, high-temperature geothermal conditions can generate entirely tensile hoop-stresses at the borehole wall. This explains the paucity of compressive failure (borehole breakout) in the TVZ case studies. In a strike-slip environment, where there is a greater difference in magnitude between the horizontal stresses, there may still be compressive failure, but the tensile region of the hoop stresses is larger in both radius on the borehole wall and magnitude.

Hoop stresses with a thermally-amplified tensile component means that more discontinuities will open at the wellbore wall than open in the reservoir and the apparent aperture will be larger. Thermal stressing is a time-dependent process, so we expect that image logs acquired after extended periods of injection to be more impacted. Damage can be differentiated from natural fractures using morphology (e.g., Figure 3B, 3C from Barton and Moos, 2010). However, it may not be possible to identify all features caused and enhanced by thermal stress at the log picking stage because high-temperature geothermal wells are extremely susceptible to this issue. In this study, we illustrate a mitigation strategy for this issue where slip tendency modelling is used to identify the sub-population of fractures that are most likely to be open beyond the thermally-enhanced stress condition at the wellbore wall.

4.2 Geologic Controls on Fracture Frequency

Geologic controls on fracture frequency generally fall into two categories: the proximity to faults and the mechanical properties of rock. However, the tectonic history of a rock will influence the fracture frequency because phases of deformation overprint through time leaving accumulated damage in their wake. Primary fractures that were generated as the rock formed, such as cooling joints in lava or welded ignimbrite, may also be present. Slip tendency modelling is useful where inherited and primary fractures are present because they may lie at an orientation that is unlikely to re-shear in the modern stress.

Proximity to faults can increase fracture frequency because the surrounding rock is damaged by the rupture. Burial depth, which dictates the magnitude of differential stress, and the scale of the fault rupture will govern the width of the damage zone. It is useful to keep damage zones in mind when evaluating image log data. If a fault lacks a well-developed core (clay gouge or breccia) or has not juxtaposed lithologies with contrasting electrical or acoustic properties, then it may only be identifiable in image logs from a localized peak in fracture frequency. The exception is if the fault moved recently and the rupture-related modification of the stress tensor magnitude and azimuth are still detectable in the pattern of drilling induced fractures and borehole breakout (e.g., Figure 6; Mandl, 2000).

As the intersection of wells with faults is a 3D problem, the angle a well approaches the fault will dictate the apparent length of this peak in fracture frequency. For example, RD-B is completed sub-parallel with, and likely within the damage zone in parts, a major fault which is interpreted from stratigraphic offset and a large surface lineament. Taking the logged interval as a whole, the fracture frequency is 1.22, which is nearly twice the frequency imaged in RD-A (0.66), which is as close as 650 m and is completed in similar lithology. Although the RD-A log has a slightly poorer image quality compared with RD-B, the difference is not enough to account for the contrast in overall fracture frequency. There is a notable lack of correlation between an overall fracture frequency and well-scale permeability, as RD-B has an injectivity that is less than half that of RD-A.

Mechanical properties dictate the likelihood a rock will respond to applied force with brittle fracture rather than ductile deformation. Working with a wide range of well case studies enables us to make some general observations about the relationship between fracture frequency and broad categories of rock type that typically have different mechanical properties. We classify the logged intervals into broad lithology categories: lava and intrusive which are brittle rocks with a high tendency for fracture, clastic rocks which have a relative tendency for ductile behaviour or shear along grain-boundaries and layers, and pyroclastic rocks which have widely various rock properties that range from something equivalent to lava to a poorly consolidated clastic rock. In future work, we plan to do this analysis with more granularity that separates these categories into lithology and alteration sub-types. Results are reported in fractures per meter, rounded to one decimal place, and means are given to one standard deviation.

Lava was imaged in two TVZ wells, yielding frequencies of 1.5 in WK-A and 5.7 in NM-B. Based on the range of fracture orientations and their relationship to the rock texture, NM-B appears to include a large population of inherited and primary fractures. Lavas at Wayang Windu geothermal field in Java, Indonesia had around 2.4 ± 0.2 fractures per meter (Masri et al., 2015), which is between the values found in our case studies. When all case studies are combined, intrusive rocks have a mean fracture frequency of 1.8 ± 0.4, with 2.1 ± 0.2 in GSF and 1.3 in the TVZ (only one occurrence). We speculate that this frequency difference may be because some of the intrusive rocks imaged in the GSF cases are Miocene-aged (i.e., a longer history of inherited fractures) while the TVZ case is Quaternary-aged, but further work is required.

Pyroclastic material is the most common category imaged and the most various in terms of rock properties. Overall fracture frequency is 0.9 ± 0.5, with 0.8 ± 0.5 in GSF and 1.2 ± 0.6 in TVZ. Given the wide variation in this category and contrasting tectonic histories, the frequencies imaged in the GSF and TVZ cases are surprisingly close. They are also comparable with the findings at Wayang Windu of ~ 1.4 (Masri et al., 2015).

The clastic category yielded the lowest fracture frequencies but was also, as expected, variable: mean of 0.5 ± 0.8 overall, with by-well variation ranging from 0.004 to 1.6 fractures per meter. The clastic rocks with extremely low fracture frequency are the only category with a strong relationship to permeability: based on MT and methylene blue analysis, they located below the smectite clay cap but still had a near-conductive thermal gradient. We can speculate that ductile deformation of this clastic unit has reduced connected primary porosity, but further work is needed to define its mechanical behaviour.

Hydrothermal alteration has a large impact on mechanical properties of rock in geothermal reservoirs (Wyering et al., 2014). Although detailed comparison with alteration is beyond the scope of this paper, the effect is present in our case studies. The pyroclastic interval in NM-A was subjected to intense phyllic alteration related to the emplacement of a large intrusive that made it harder and more likely to sustain brittle fracture. Frequency in this interval is 1.9 and removing it from the aggregated data reduces mean frequency for TVZ pyroclastics from 1.2 +/- 0.6 to 0.8 ± 0.1.

5. SLIP TENDENCY MODELLING

Identifying those fractures that are likely to be open beyond the borehole wall is a key step in using these data to quantify the geologic mechanisms that control permeability. As discussed above, thermally-enhanced hoop stresses at the borehole wall cause a larger proportion of fractures to be open than would be the case in the reservoir (e.g., Figure 3C).

We use slip tendency to identify the population of fractures that may be open in the reservoir. Fractures with high slip tendency are at an orientation (strike and dip) where they are more likely to experience shear failure given the magnitude and orientation of the effective stress tensor, where the effective stress tensor is the maximum σ_1, intermediate σ_2, and minimum σ_3 tectonic stresses minus the oppositional force of pore fluid pressure. The case study is located in a district where normal faulting dominates, such that $\sigma_1 = S_v$, $\sigma_2 = S_{Hmax}$ and $\sigma_3 = S_{hmin}$, but the magnitudes of σ_2 and σ_3 may be similar (Figure 5). Because asperities on the fracture surface become mismatched, shear failure generates new self-propping permeability. Repeated failure is critical for maintaining fracture permeability in high-temperature, convecting geothermal reservoirs because active hydrothermal mineral precipitation destroys open space.

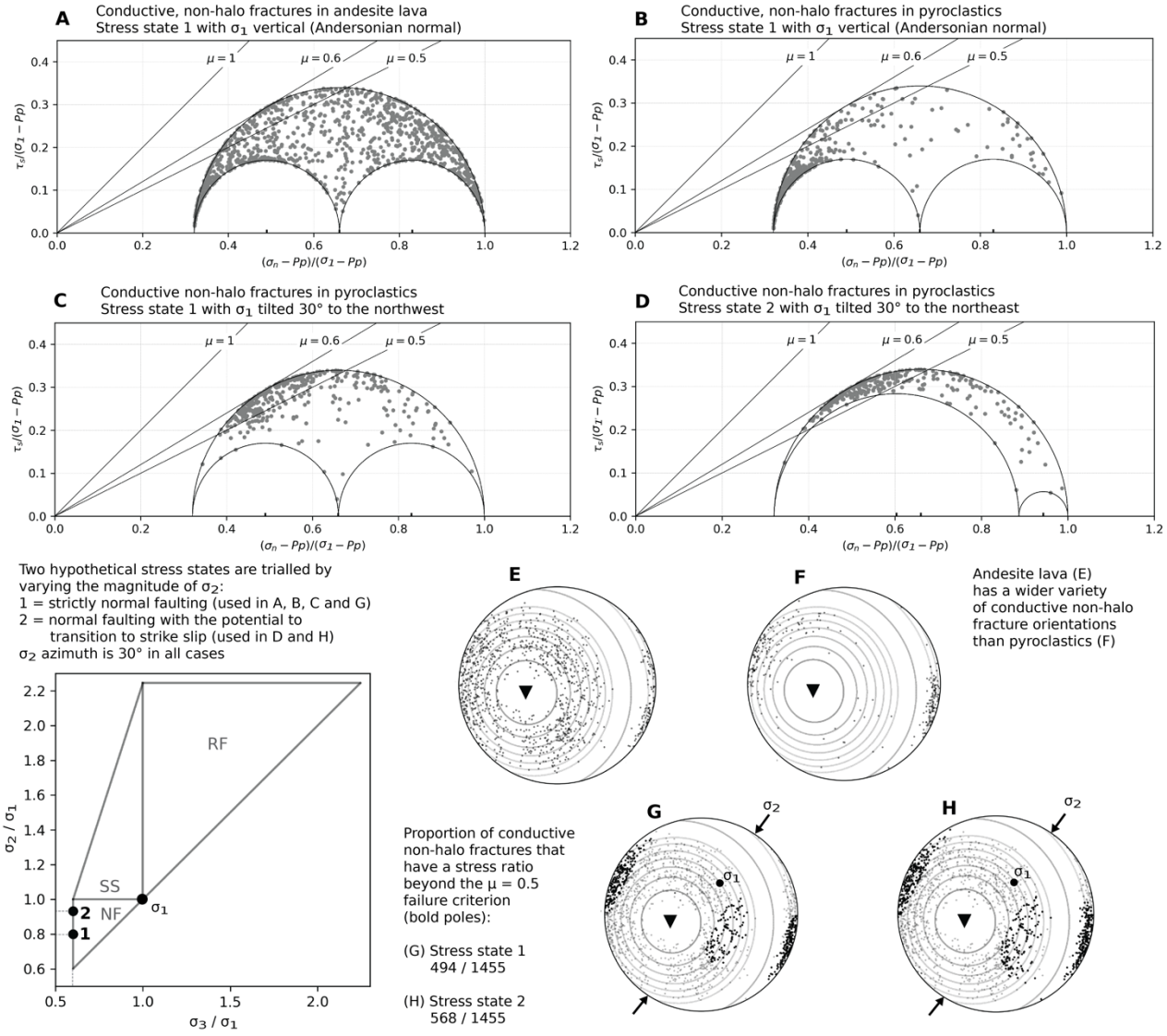

Figure 5: Possible open fractures (conductive non-halo) from NM-B projected in 3D Mohr space using two stress tensor magnitude and two scenarios (four total, with three presented here) to model slip tendency of the fracture populations. Results are presented twice, once in Mohr space and once on a stereonet: A (E) and B (F) illustrate the impact of lithology; C (G) and D (H) illustrate the effect of changing the magnitude of σ_2 (stress state 1 and 2) but both have σ_1 tilted to the NW, which projects into the NE quadrant in these lower hemisphere stereonet projections.

Barton et al. (1995) established that imaged fractures with a high slip tendency closely correlate with wellbore scale fluid flux in low permeability settings outside geothermal systems (e.g., deep scientific boreholes and potential nuclear waste storage sites). Similar methods were applied at Dixie Valley Geothermal System (Hickman et al., 1997; Hickman et al., 1998) and on marginal, low permeability wells at Coso Geothermal System (Davatzes and Hickman, 2010b). They generated insight into geologic controls on permeability at both the wellbore and reservoir scale.

To illustrate slip tendency modelling, we explored a range of stress magnitude and orientation cases for one case study (Figure 6). We found that of the total 1455 fractures identified in the image log as possibly permeable based on the likely absence of mineral fills, 494-568 have a relatively high ratio of shear to normal stress given the geomechanical model parameters used. Note that we cannot distinguish which of the non-haloed conductive fractures are filled with water and which are filled with clay.

We constrained reasonable model parameters using the tectonic conditions of the TVZ context and moment tensor inversions for micro-seismic events generated during thermal stimulation in this case study reservoir (Hopp et al., 2019). We derive the in-situ stress tensor cases using modelling methods described in Zoback (2010) and approximate S_{hmin} (which is σ_3 in this case study) using the Coulomb Failure Criterion (Byerlee, 1978). Comparison between this criterion (with $\mu = 0.5$) and extended leak-off tests found it to be a reasonable fit and, therefore, it is likely that fracturing controls minimum stress in a TVZ geothermal reservoir (Wallis et al., Submitted). We rotate each stress tensor onto the fractures to find applied shear (τ) and normal (σ_n) stresses using the method in Barton et al. (1995). While improving constraints on the geomechanical model for NM-B and the other six case studies is underway, it is difficult to generate high-confidence, single realization of these models for geothermal wells in active volcano-tectonic settings. This is because stress varies over short distances (e.g., the stress tensor rotations in Figure 6) and the data required to constrain these models are infrequently acquired during geothermal drilling.

6. COMPARING FREQUENCY TO FEEDZONES

When plotted by depth and combined with geologic context, the slip tendency modelling reveals possible explanatory mechanisms for two of the three FZ in NM-B and textural analysis of the image explains the presence of a third. But before detailing these results, we describe two concepts that underly the interpretation: the evidence of active faulting provided by drilling induced tensile fractures and the likelihood that the various stress model scenarios are correct.

As already discussed above, the way the stress tensor resolves onto the borehole wall generates compressive and tensile hoop stresses that create drilling induced damage to the borehole wall: borehole breakout (compressive failure) and tensile fractures. If one component of the stress tensor and the borehole are aligned, then the azimuth of the stress tensor can be read directly from the azimuth of drilling induced damage.

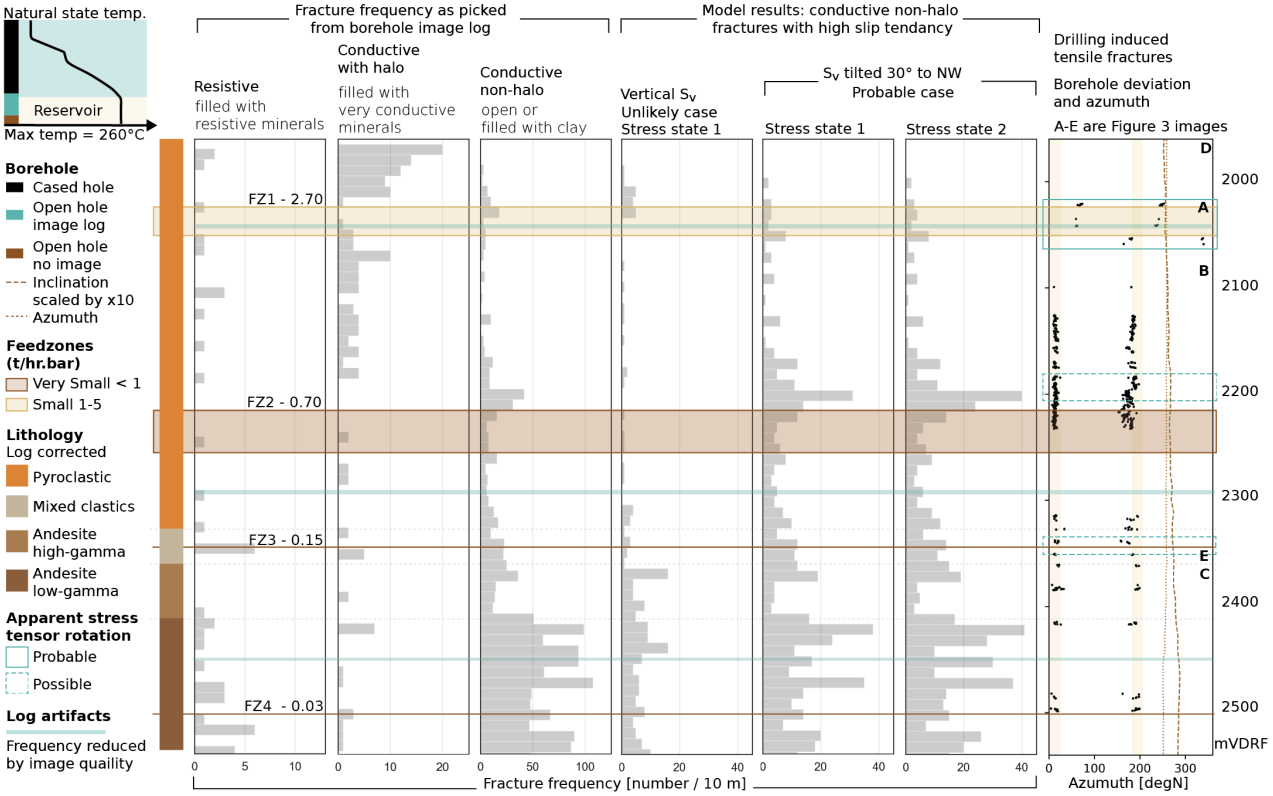

Figure 6: Fractures picked from the NM-B image log and the slip tendency model results from Figure 6 compared with distribution of FZ interpreted from the completion test. Posted injectivity value (t/hr.bar) is total well II split by % contribution as determined using a wellbore model of the completion test. Examples from Figure 3 are plotted by letter.

As it is common to assume that one component of the stress tensor is vertical, this leads to the rule of thumb that drilling induced damage in vertical wells directly equates to the orientation of the horizontal components of the stress tensor. However, our modelling indicates that the stress tensor may be inclined. Furthermore, stress resolved onto an inclined borehole, as is the case in NM-B, means that deconvolution is required to determine the stress tensor azimuth from drilling induced damage (Peška and Zoback, 1995). Despite not reflecting the true azimuth of the stress tensor, we can read relative azimuth from drilling induced damage in an inclined borehole provided borehole deviation and azimuth are held steady. If this condition is met, then a rotation of tensile fracture azimuth equates to a rotation in the stress tensor (Figure 6).

NM-B is an inclined borehole and, as will be discussed below, it is likely that σ_1 is not vertical. However, the inclination and azimuth of the borehole are generally consistent and there are many tensile fractures that we can use to observe the stress tensor variation with depth. At FZ1, tensile fractures are rotated > 40° from the typical azimuth and the switch in orientation occurs over < 20 m, which is characteristic of an active fault. There are two other more subtle rotations in tensile fracture azimuth, one above FZ2 and another coincident with FZ3. As these are smaller features and because the one coincident with FZ3 is located within a layered clastic unit, it is not clear if they are caused by fault rupture, laminated anisotropic lithology, or that the suitable variation in wellbore deviation has been sufficient to alter the azimuth of tensile fractures. This will be the subject of further research.

Uncertainty in stress tensor orientation had a great impact on the slip tendency modelling, more so than varying the magnitude of maximum horizontal stress (which is σ_2 in this case study). As can be seen in Figure 5B, the case where σ_1 is vertical requires the majority of fractures in the pyroclastic interval to be Mode 1 (purely tensile) or Mode 2 (combine tensile and shear) openings. This seems unlikely given that the well is completed into a Holocene-active fault zone that has been resolved with both surface mapping and microseismicity. The lack of any discernible relationship between stress tensor rotations in NM-B and the high slip tendency fractures modelled using a vertical σ_1 also indicates that this case may not reflect in situ conditions. By contrast, the two cases with σ_1 tilted 30º NW (Figure 5 C and D), are both consistent with fracture formation by shear failure and the location of stress rotation.

A large proportion of the fractures in the low-gamma andesite did not have a high slip tendency (Figure 6). We expected this result because primary fractures, such as cooling joints, are common in andesite lava and we observed a great number of thermally-enhanced hoop stress induced fractures throughout the andesite (Figure 3C). Where identified, the latter are not included in the non-halo conductive fracture dataset.

Fractures with high slip tendency in the pyroclastic unit formed two clusters that are coincident with stress tensor rotations. It is likely that these clusters are fault damage zones. Based on the orientation of the fault, FZ1 is located in the hanging wall which is consistent with the distribution of fault-related permeability (open-space mineralisation) observed in fossil geothermal systems (Rhys et al., 2020). FZ2 overlaps with lower cluster of fractures with high slip tendency but because a distinct fault plane is not present in this zone, further work is required to constrain a structural conceptual model.

Two very small FZ appear as discrete features in the completion test data. FZ3 corelates with a thin clastic unit that was identified using the texture of the micro-resistivity log (c.f., Figure 3). This unit is a series of rocky soils and stream deposits, like what would be found on the flanks of Mt Taranaki today. It is challenging to resolve units like these using cuttings because grinding it into small rock chips (< 5 mm) makes it near-indistinguishable from the andesite lava it came from. No discrete geologic mechanism has been revealed for FZ4, as we have discovered no clear difference between the geology at the position of this FZ and the rock around it. However, this FZ is tiny and, as described Section 2, deep FZ are typically over-emphasized by completion testing.

The final step in image log analysis is a robust integration of the interpretation with the reservoir-scale context, but it is beyond the scope of this paper. A robust integration is valuable to the operator because it enables them to ascertain how well the imaged interval reflects processes in the reservoir as a whole and, therefore, how conclusions may be applied to resource decisions.

7. CONCLUDING REMARKS

The work presented here is part of ongoing research into the geologic controls on fluid flow in high-temperature geothermal reservoirs across a range of spatial scales. Herein we describe methodological concerns for using image log data to quantify which geologic features influence the position of high-flux zones (FZ) at the wellbore scale. We illustrated how fracture frequency and orientation data picked from an image log benefits from additional treatment prior to use in interpretation to quantify data integrity, sample bias and the population of fractures that are likely to be open beyond the borehole wall. If this is done and the results are compared with FZ in a manner that considers the uncertainty inherent in well testing, the mechanisms controlling FZ distribution may become clear. We expect that applying the methodologies described here on our seven case studies will reveal a range of geologic controls on FZ that can be used as interpretive analogies elsewhere.

OPEN SOURCE CONTRIBUTION

An opensource Python package accompanies this paper: https://github.com/ICWallis/fractoolbox. This research uses packages in the SciPy ecosystem (Virtanen et al., 2020) and mplstereonet (Kington, 2020).

ACKNOWLEDGEMENTS

Irene Wallis received funding from a University of Auckland Doctoral Scholarship. The authors thank companies who provided data: Supreme Energy, Mercury, and Contact Energy. We also thank the company and rig-site staff, wireline engineers, and log analysts who acquired and processed raw data. The authors acknowledge Mohamed Alboub (Schlumberger) for the insightful conversations and FMI tool expertise. We thank Evert Quintero for the 3D Mohr plot code. Schlumberger provided Techlog and Advanced Logic Technology provided WellCAD for this research.

REFERENCES

Baroek, M., Stimac, J., Sihotang, A. M., Putra, A. P., and Martikno, R., 2018, Formation and fracture characterization of the Muara Laboh Geothermal System, Sumatra, Indonesia, Geothermal Resources Council Transactions, Volume 42: Reno, Nevada.

Barton, C. A., and Moos, D., 2010, Geomechanical wellbore imaging: Key to managing the asset life cycle, *in* Pöppelreiter, C., García-Carballido, C., and Kraaijveld, M., eds., Dipmeter and Borehole Image Log Technology, p. 81-112.

Barton, C. A., Zoback, M. D., and Moos, D., 1995, Fluid flow along potentially active faults in crystalline rock: Geology, v. 23, p. 683-686.

Bixley, P. F., Clotworthy, A. W., and Mannington, W. I., 2009, Evolution of the Wairakei geothermal reservoir during 50 years of production: Geothermics, v. 38, no. 1, p. 145-154.

Byerlee, J., 1978, Friction of rocks: Pure and Applied Geophysics PAGEOPH, v. 116, no. 4-5, p. 615-626.

Chambefort, I., Buscarlet, E., Wallis, I. C., Sewell, S., and Wilmarth, M., 2016, Ngatamariki Geothermal Field, New Zealand: Geology, geophysics, chemistry and conceptual model: Geothermics, v. 59, p. 266-280.

Davatzes, N. C., and Hickman, S. H., 2010a, The feedback between stress, faulting and fluid folw: lessons from the Coso Geothermal Field, CA, USA, Proceedings World Geothermal Congress: Bali, Indonesia.

-, 2010b, Stress, fracture, and fluid-flow analysis using acoustic and eletrical image logs in hot fractured granites of the Coso Geothermal Field, California, U.S.A, *in* Pöppelreiter, C., García-Carballido, C., and Kraaijveld, M., eds., Dipmeter and Borehole Image Log Technology, p. 159-293.

Durán, E. L., Adam, L., Wallis, I. C., and Barnhoorn, A., 2019, Mineral Alteration and Fracture Influence on the Elastic Properties of Volcaniclastic Rocks: Journal of Geophysical Research: Solid Earth, v. 124, no. 5, p. 4576-4600.

Ellis, S., Heise, W., Kissling, W., Villamor, P., and Schreurs, G., 2014, The effect of crustal melt on rift dynamics: Case study of the Taupo Volcanic Zone: New Zealand Journal of Geology and Geophysics, v. 57, no. 4, p. 453-458.

Halwa, L., Wallis, I. C., and Lozada, G. T., 2013, Geological analysis of the volcanic subsurface using borehole resistivity images in the Ngatamariki Geothermal Field, New Zealand, 35th New Zealand Geothermal Workshop: Rotorua.

Hanano, M., 2004, Contribution of fractures to formation and production of geothermal resources: Renewable and Sustainable Energy Reviews, v. 8, no. 3, p. 223-236.

Hickman, S., Barton, C., Zoback, M., Morin, R., Sass, J., and Benoit, R., 1997, In-situ stress and fracture permeability in a fault-hosted geothermal reservoir at Dixie Valley, Nevada, Geothermal Resources Council Transactions, Volume 21: Burlingame, California, p. 181-189.

Hickman, S., Zoback, M., and Benoit, R., 1998, Tectonic controls on fault-zone permeability in a geothermal reservoir at Dixie Valley, Nevada, Proceedings of the SPE/ISRM Rock Mechanics in Petroleum Engineering Conference, Volume 1, p. 79-83.

Hopp, C., Sewell, S., Mroczek, S., Savage, M., and Townend, J., 2019, Seismic Response to Injection Well Stimulation in a High-Temperature, High-Permeability Reservoir: Geochemistry, Geophysics, Geosystems, v. 20, no. 6, p. 2848-2871.

Jaeger, J. C., Cook, N. G. W., and Zimmerman, R. W., 2007, Fundementals of Rock Mechanics, Malden, MA, USA, Blackwell Publishing.

Kington, J., 2020, mplstereonet: GitHub.

Mandl, G., 2000, Faulting in Brittle Rocks An Introduction to the Mechanics of Tectonic Faults, Berlin, Heidelberg, Berlin, Heidelberg : Springer Berlin Heidelberg 2000.

Masri, A., Barton, C. A., Hartley, L., and Ramadhan, Y., 2015, Structural permeability assessment using geological structural model integrated with 3D geomechanical study and discrete facture network model in Wayang Windu Geothermal Field, West Java, Indonesia, Proceedings Fourtieth Workshop on Geothermal Reservoir Engineering, Volume SGP-TR-204: Stanford University, Stanford, California.

Massiot, C., McLean, K., McNamara, D., Sepulveda, F., and Milicich, S. D., 2017a, Discussion between a reservior engineer and a geologist: Permeability identification from compleation test data and borehole image logs intergration, New Zealand Geothermal Workshop.

Massiot, C., Nicol, A., McNamara, D. D., and Townend, J., 2017b, Evidence for tectonic, lithologic, and thermal controls on fracture system geometries in an andesitic high-temperature geothermal field: Journal of Geophysical Research: Solid Earth, v. 122, no. 8, p. 6853-6874.

McNamara, D., Bannister, S., Villamor, P., Sepulveda, F., Milicich, S. D., Alcaraz, S. A., and Massiot, C., 2016, Exploring structure and stress from depth to surface in the Wairakei Geothermal Field, New Zealand, Stanford Geothermal Workshop.

McNamara, D. D., Massiot, C., Lewis, B., and Wallis, I. C., 2015, Heterogeneity of structure and stress in the Rotokawa Geothermal Field, New Zealand: Journal of Geophysical Research: Solid Earth, v. 120, no. 2, p. 1243-1262.

McNamara, D. D., Milicich, S. D., Massiot, C., Villamor, P., McLean, K., Sépulveda, F., and Ries, W. F., 2019, Tectonic Controls on Taupo Volcanic Zone Geothermal Expression: Insights From Te Mihi, Wairakei Geothermal Field: Tectonics, v. 38, no. 8, p. 3011-3033.

Mussofan, W., Stimac, J. A., Baroek, M., Colvin, A., Sidik, R. P., Ganefianto, N., and Santana, S., 2019, Thick silicic volcanic sequences at Muara Laboh and Rantau Dedap geothermal fields, Sumatra, Indonesia: Implications for reservior architecture and permeability, Proceedings 41st New Zealand Geothermal Workshop: Auckland, New Zealand.

ISSN 2703-4275

Nemčok, M., Moore, J. N., Christensen, C., Allis, R., Powell, T., Murray, B., and Nash, G., 2007, Controls on the Karaha–Telaga Bodas geothermal reservoir, Indonesia: Geothermics, v. 36, no. 1, p. 9-46.

Peška, P., and Zoback, M. D., 1995, Compressive and tensile failure of inclined well bores and determination of in situ stress and rock strength: Journal of Geophysical Research: Solid Earth, v. 100, no. B7, p. 12791-12811.

Priest, S., 1993, Discontinuity Analysis for Rock Engineering, Netherlands, Springer.

Rhys, D. A., Lewis, P. D., and Rowland, J. V., 2020, Structural controls on ore localization in epithermal gold-silver deposits: A mineral systems approch: Reviews in Economic Geology, v. 21, no. 83-145.

Rosenberg, M. D., Wilson, C. J. N., Bignall, G., Ireland, T. R., Sepulveda, F., and Charlier, B. L. A., 2020, Structure and evolution of the Wairakei–Tauhara geothermal system (Taupo Volcanic Zone, New Zealand) revisited with a new zircon geochronology: Journal of Volcanology and Geothermal Research, v. 390.

Rowland, J. V., and Sibson, R. H., 2004, Structural controls on hydrothermal flow in a segmented rift system, Taupo Volcanic Zone, New Zealand: Geofluids, v. 4, no. 4, p. 259-283.

Sepulveda, F., Rosenberg, M. D., Rowland, J. V., and Simmons, S. F., 2012, Kriging predictions of drill-hole stratigraphy and temperature data from the Wairakei geothermal field, New Zealand: Implications for conceptual modeling: Geothermics, v. 42, p. 13-31.

Sidik, R. P., Mussofan, W., Santana, S., and Azis, H., 2016, Structure geology of southwestern sector Rantau Dedap Geothermal Field, Proceedings Annual 4th Indonesia International Geothermal Convention & Exhibition: Jakarta, Indonesia.

Sidik, R. P., Mussofan, W., Wallis, I. C., Azis, H., Stimac, J. A., and Ganefianto, N., 2018, Two contrasting geothermal fields in Sumatra, Indonesia: Muara Laboh and Rantau Dedap, New Zealand Geothermal Workshop: Taupo.

Sieh, K., and Natawidjaja, D., 2000, Neotectonics of the Sumatran Fault, Indonesia: Journal of Geophysical Research: Solid Earth (1978–2012), v. 105, no. B12, p. 28295-28326.

Stimac, J., Ganefianto, N., Baroek, M., Sihotang, M., Ramadhan, I., Mussofan, W., Sidik, R., Alfiady, Dyaksa, D. A., Azis, H., Putra, A. P., Martikno, R., Irsamukhti, R., Santana, S., Matsuda, K., Hatanaka, H., Soeda, Y., Cariou, L., and Egermann, P., 2019a, An overview of the Muara Laboh geothermal system, Sumatra: Geothermics, v. 82, p. 150-167.

Stimac, J., Sihotang, A. M., Mussofan, W., Baroek, M., Jones, C., Moore, J. N., and Schmitt, A. K., 2019b, Geologic controls on the Muara Laboh geothermal system, Sumatra, Indonesia: Geothermics, v. 82, p. 97-120.

Stimac, J. A., Baroek, M., Suminar, A., and Sagala, B., 2010, Integration of surface and well data to determine structural controls on permeability at Salak (Awibengkok), Indonesia, Proceedings World Goethermal Congress Bali, Indonesia.

Terzaghi, R. D., 1965, Sources of error in joint surveys: Geotechnique, v. 15, no. 3, p. 287-304.

Virtanen, P., Gommers, R., Oliphant, T. E., Haberland, M., Reddy, T., Cournapeau, D., Burovski, E., Peterson, P., Weckesser, W., Bright, J., Walt, S. J. v. d., Brett, M., Wilson, J., Millman, K. J., Mayorov, N., Nelson, A. R. J., Jones, E., Kern, R., Larson, E., Carey, C., Polat, İ., Feng, Y., Moore, E. W., VanderPlas, J., Laxalde, D., Perktold, J., Cimrman, R., Henriksen, I., Quintero, E. A., Harris, C. R., Archibald, A. M., Ribeiro, A. H., Pedregosa, F., Mulbregt, P. v., and Contributors, S., 2020, SciPy 1.0: Fundamental Algorithms for Scientific Computing in Python: Nature Methods, v. in press.

Wallis, I. C., McCormick, S., Sewell, S., and Boseley, C., 2012, Formation assessment in geothermal using wireline tools - application and early results from the Ngatamariki Geothermal Field, New Zealand, New Zealand Geothermal Workshop: Rotorua.

Wallis, I. C., Pye, D. S., Dempsey, D. E., and Rowland, J. V., Submitted, A users guide to leak-off test procedures and interpretation for geothermal wells, 2021 World Geothermal Congress: Reykjavik, Iceland.

Wallis, I. C., Rowland, J. V., and Dempsey, D. E., 2018, The relationship between geothermal fluid flow and geologic context: A global review, GRC Transactions, Volume Vol. 42: Reno, Nevada.

Wilson, C. J. N., and Rowland, J. V., 2016, The volcanic, magmatic and tectonic setting of the Taupo Volcanic Zone, New Zealand, reviewed from a geothermal perspective: Geothermics, v. 59, p. 168-187.

Wyering, L. D., Villeneuve, M. C., Wallis, I. C., Siratovich, P. A., Kennedy, B. M., Gravley, D. M., and Cant, J. L., 2014, Mechanical and physical properties of hydrothermally altered rocks, Taupo Volcanic Zone, New Zealand: Journal of Volcanology and Geothermal Research, v. 288, no. 0, p. 76-93.

Zarrouk, S. J., and McLean, K., 2019, Geothermal well test analysis : fundamentals, applications and advanced techniques, London : Academic Press. 2019.

Zoback, M. D., 2010, Reservoir Geomechanics, Cambridge University Presss